Electronic Supplementary Material (ESI) for Dalton Transactions

Supporting Information of

Coordination site-Dependent Cation Binding and Multi-responsible Redox Properties of Janus-Head Metalloligand, $[Mo^{V}(1,2\text{-mercaptophenolato})_3]^{-}$

Takeshi Matsumoto,[b] Masanori Wakizaka,[a] Hirokazu Yano,[a] Atsushi Kobayashi,[a] Ho-Chol Chang,*[a] and Masako Kato*[a,b]

[a] *Division of Chemistry, Faculty of Science, Hokkaido University, North-10, West-8, Kita-ku, Sapporo 060-0810, Japan. Fax: +81-11-706-3447; Tel: +81-11-706-3817; E-mail: mkato@sci.hokudai.ac.jp.*

[b] *Center for Strategic Utilization of Elements, Faculty of Science, Hokkaido University, North-10, West-8, Kita-ku, Sapporo 060-0810, Japan.*

Contents.

20. **Figure 11S.** UV-vis-NIR spectra, CVs, and DPVs of **1**-**3** in *o*-$Cl_2C_6H_4$ solution containing 0.05 M TBAP.

21. **Table 7S.** Redox potentials of **1**, **2**, and **3** in CH_3CN solution containing 0.05 M TBAFB.

Synthesis of Fe^{II}-powder sample. A dark brown MeOH (0.7 mL) solution of **1** (25 mg, 0.039 mmol) was added to a pink MeOH (0.3 mL) solution of $Fe^{II}Cl_2{\cdot}4H_2O$ (15.5 mg, 0.078 mmol). After stirring for 1 hour, a reddish-brown precipitate was obtained. This was filtered, and washed with H_2O (0.5 mL × 2) and MeOH (0.3 mL × 2). The resulting reddish-brown powder was dried in vacuo and used for UV-vis-NIR measurements as Fe^{II}-powder sample.

Synthesis of $\{Co^{II}(H_2O)(MeOH)[fac\text{-}Mo^{V}(mp)_3]_2\}{\cdot}1.5CH_2Cl_2$ ($4{\cdot}1.5CH_2Cl_2$). A dark brown MeOH (5 mL) solution of **1** (200 mg, 0.315 mmol) was added to a pink MeOH (1 mL) solution of $Co^{II}Cl_2{\cdot}4H_2O$ (125 mg, 0.632 mmol). After stirring for 1 hour, a reddish-brown precipitate was obtained. This was filtered, and washed with H_2O (3 mL × 2) and MeOH (1 mL × 2). The resulting reddish-brown powder was dried in vacuo and used for UV-vis-NIR measurements as Co^{II}-powder sample. For synthesis of crystal sample suitable for X-ray crystallographic analysis, this powder sample was dissolved in CH_2Cl_2 (20 mL), then *n*-hexane (20 mL) was layered onto this solution. After storage of this solution for 5 days at room temperature, reddish-brown crystals were obtained. After filtration and washing with *n*-hexane (2 mL × 3), followed by drying in vacuo, complex $\mathbf{4}{\cdot}1.5CH_2Cl_2$ was isolated as reddish-brown crystals in 10% yield. Anal. Found: C, 39.21; H, 2.86. Calc. for $C_{38.5}H_{33}Cl_3CoMoO_8S_6$ ($\mathbf{4}{\cdot}1.5CH_2Cl_2$): C, 39.41; H, 2.86%. $\chi_M T_{300K}$ = 4.515 emu·K·mol^{-1}.

Synthesis of Ni^{II}-powder sample. A dark brown MeOH (0.7 mL) solution of **1** (25 mg, 0.039 mmol) was added to a pink MeOH (0.3 mL) solution of $Ni^{II}Cl_2{\cdot}4H_2O$ (18.5 mg, 0.078 mmol). After stirring for 1 hour, a reddish-brown precipitate was obtained. This was filtered, and washed with H_2O (0.5 mL × 2) and MeOH (0.3 mL × 2). The resulting reddish-brown powder was dried in vacuo and used for UV-vis-NIR measurements as Ni^{II}-powder sample.

Table 1S. Crystallographic data for **4**·1.5CH_2Cl_2.

	4·1.5CH_2Cl_2
formula	$C_{38.5}H_{33}Cl_3CoMo_2O_8S_6$
fw	1173.21
crystal size (mm^3)	0.05× 0.05× 0.05
crystal system	triclinic
space group	*P*-1(No. 2)
a(Å)	11.356(2)
b(Å)	13.024(2)
c(Å)	14.982(3)
α(°)	96.542(3)
β(°)	106.062(3)
γ(°)	95.802(3)
V($Å^3$)	2095.0(6)
T(K)	163
Z	2
D_{calc}(g cm^{-3})	1.860
F(000)	1172
μ(Mo Kα)(cm^{-1})	15.223
measured reflns.	14583
unique reflns.	9140
refined parameters	533
GOF on F^2	1.014
R_{int}	0.025
R_1[a]	0.0534
wR_2[b] (all data)	0.1418

[a] $R_1 = \Sigma||F_o| - |F_c||/\Sigma|F_o|$. [b] $wR_2 = \{[\Sigma w(F_o^2 - F_c^2)^2]/[\Sigma w(F_o^2)^2]\}^{1/2}$.

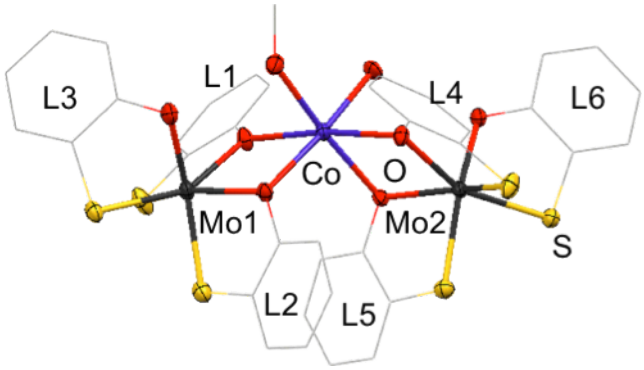

Figure 1S. Asymmetric unit of **4**·1.5CH_2Cl_2 with thermal ellipsoid plots for Mo (black), O (red), S (yellow), and Co (blue) (50% probability). Hydrogen atoms and solvent molecules are omitted, and carbon atoms are depicted as wireframe for clarity.

The complex **4**·1.5CH_2Cl_2 is isomorphous with the **3**·1.5CH_2Cl_2.

Chart 1S. Definitions of OCT/TP(%) criteria.

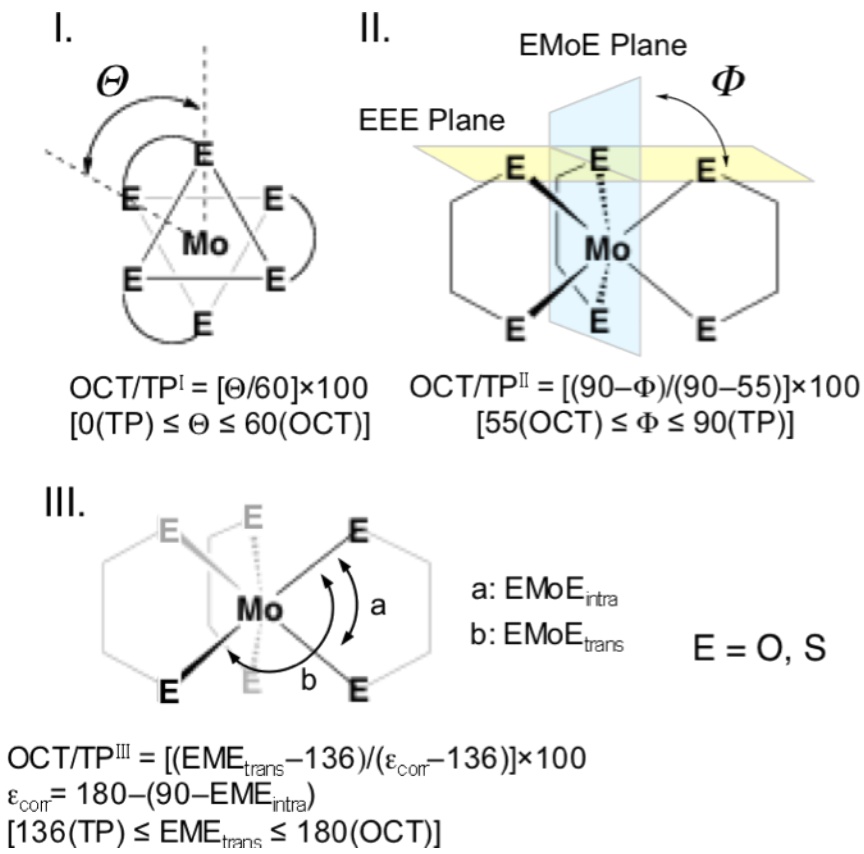

Table 2S. Geometrical parameters for **1**-**5**.

		OCT/TP^{I}	OCT/TP^{II}	OCT/TP^{III}
1		43.4	45.3	50.7
2		50.5	54.0	49.5
3·1.5CH_2Cl_2	Mo1	38.2	39.6	45.0
	Mo2	44.6	46.7	51.6
4·1.5CH_2Cl_2	Mo1	36.4	37.7	41.3
	Mo2	43.5	45.3	50.1
5		63.5	68.8	76.2

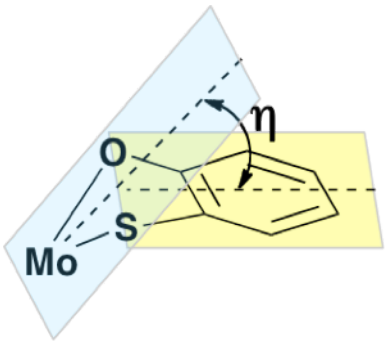

Table 3S. Bending angles (η) in mp^{2-} of **1**-**5**.

	η / °				
	1	**2**	**3**·1.5CH_2Cl_2	**4**·1.5CH_2Cl_2	**5**
L1	9.27*	7.60	4.48*	4.43*	11.32*
L2	9.27*	6.60	18.92*	20.55*	9.26*
L3	9.27*	18.0	10.99	10.60	3.35*
L4			3.19*	2.81*	
L5			16.57*	18.34*	
L6			9.58	9.47	
Average	9.27	10.73	10.62	11.03	7.98

* Ligands directly attached to Na (**1**), Mn (**3**·1.5CH_2Cl_2), Co (**4**·1.5CH_2Cl_2), or Cu (**4**) atoms.

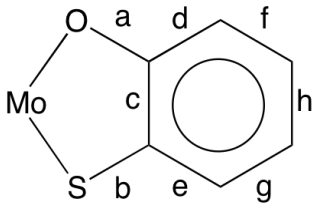

Table 4S. Bond distances (Å) of the mp^{2-} in **1**-**5**.

		Å							
		a	b	c	d	e	f	g	h
1	L1*	1.361(4)	1.749(4)	1.375(6)	1.396(6)	1.429(5)	1.406(6)	1.384(8)	1.402(8)
2	L1	1.336(3)	1.746(3)	1.399(4)	1.393(4)	1.400(4)	1.384(5)	1.377(5)	1.387(6)
	L2	1.337(3)	1.748(3)	1.394(4)	1.399(4)	1.387(4)	1.378(5)	1.385(5)	1.382(6)
	L3	1.343(3)	1.751(3)	1.393(4)	1.397(4)	1.395(4)	1.378(4)	1.388(4)	1.385(5)
	Av.	1.339(3)	1.748(3)	1.395(4)	1.396(4)	1.394(4)	1.380(5)	1.383(5)	1.385(6)
3·1.5CH_2Cl_2	L1*	1.367(7)	1.748(6)	1.395(7)	1.386(8)	1.397(9)	1.391(9)	1.374(9)	1.390(8)
	L2*	1.374(6)	1.751(5)	1.396(6)	1.395(8)	1.400(7)	1.378(8)	1.373(9)	1.386(7)
	L3	1.347(7)	1.749(5)	1.406(7)	1.396(7)	1.393(9)	1.395(9)	1.387(7)	1.390(8)
	L4*	1.363(6)	1.755(6)	1.409(8)	1.390(8)	1.399(9)	1.386(8)	1.381(10)	1.389(10)
	L5*	1.374(5)	1.740(5)	1.405(7)	1.377(7)	1.406(6)	1.387(6)	1.367(9)	1.394(8)
	L6	1.344(7)	1.740(5)	1.401(7)	1.389(7)	1.406(8)	1.380(9)	1.380(8)	1.396(8)
	Av.	1.362(6)	1.747(5)	1.402(7)	1.389(8)	1.400(8)	1.386(8)	1.378(9)	1.391(8)
4·1.5CH_2Cl_2	L1*	1.361(7)	1.755(6)	1.401(6)	1.393(8)	1.388(8)	1.400(8)	1.370(8)	1.388(7)
	L2*	1.375(6)	1.749(5)	1.386(6)	1.395(7)	1.397(7)	1.376(8)	1.377(8)	1.396(7)
	L3	1.341(7)	1.748(5)	1.419(6)	1.387(7)	1.395(8)	1.390(9)	1.388(7)	1.388(7)
	L4*	1.364(6)	1.750(6)	1.397(7)	1.382(7)	1.411(8)	1.384(8)	1.372(9)	1.388(9)
	L5*	1.363(4)	1.746(5)	1.411(7)	1.386(7)	1.389(6)	1.379(6)	1.396(8)	1.396(8)
	L6	1.360(7)	1.752(5)	1.376(7)	1.398(7)	1.401(8)	1.375(8)	1.371(8)	1.398(8)
	Av.	1.361(6)	1.750(5)	1.398(7)	1.390(7)	1.397(8)	1.384(8)	1.379(8)	1.392(8)
5	L1*	1.352(6)	1.765(5)	1.395(7)	1.402(7)	1.386(7)	1.381(8)	1.383(8)	1.387(9)
	L2*	1.338(5)	1.754(5)	1.413(7)	1.400(7)	1.393(7)	1.396(8)	1.378(8)	1.363(9)
	L3*	1.349(5)	1.748(4)	1.396(7)	1.382(6)	1.402(7)	1.382(7)	1.396(7)	1.379(8)
	Av.	1.346(5)	1.756(5)	1.401(7)	1.395(7)	1.394(7)	1.386(8)	1.386(8)	1.376(9)

* Ligands directly attached to Na (**1**), Mn (**3**·1.5CH_2Cl_2), Co (**4**·1.5CH_2Cl_2), or Cu (**5**) atoms.

Table 5S. Selected bond distances (Å) for **4**·1.5CH_2Cl_2.

	4·1.5CH_2Cl_2
Mo(1)-O(1) [L1]	2.065(4)*
Mo(1)-O(2) [L2]	2.072(3)*
Mo(1)-O(3) [L3]	2.021(3)
Mo(2)-O(4) [L4]	2.063(3)*
Mo(2)-O(5) [L5]	2.068(3)*
Mo(2)-O(6) [L6]	2.017(3)
Mo(1)-S(1) [L1]	2.3224(15)
Mo(1)-S(2) [L2]	2.3190(12)
Mo(1)-S(3) [L3]	2.3490(15)
Mo(2)-S(4) [L4]	2.3297(14)
Mo(2)-S(5) [L5]	2.3033(12)
Mo(2)-S(6) [L6]	2.3559(15)

* Distances between the Mo and chalcogen atoms directly attached to Co^{II} atom.

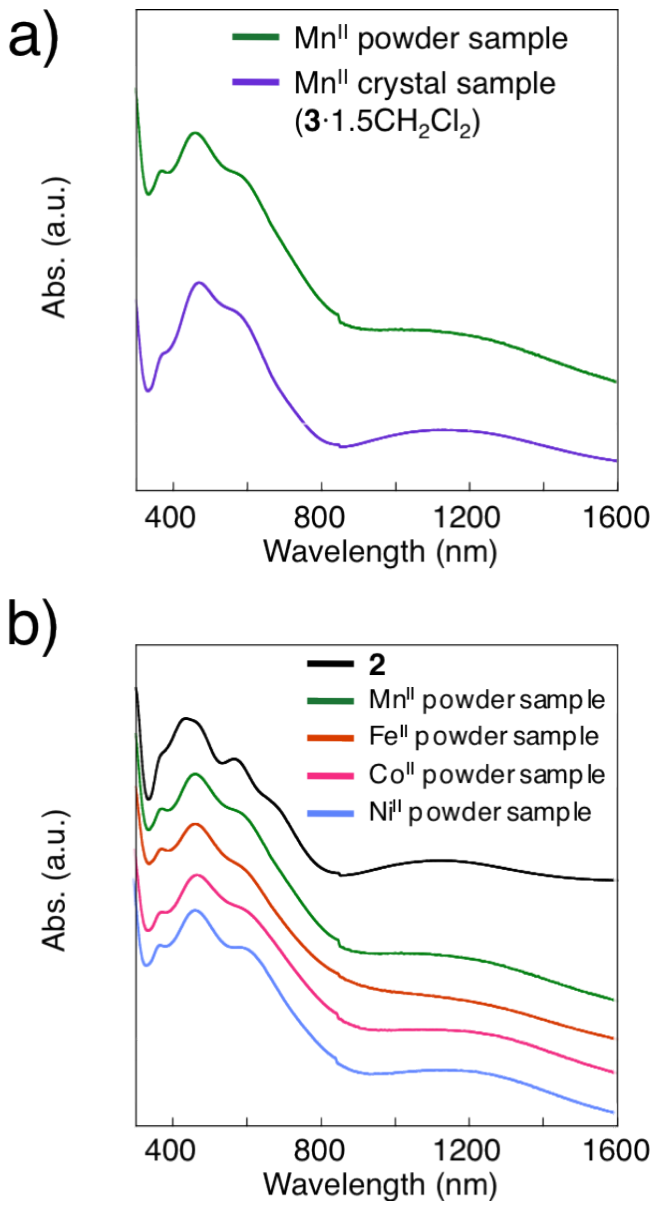

Figure 2S. (a) UV-Vis-NIR spectra of Mn^{II} powder sample (green line) and Mn^{II} crystal sample (purple line), and (b) **2** (black line), Mn^{II} powder sample (green line), Fe^{II} powder sample (orange line), Co^{II} powder sample (pink line), and Ni^{II} powder sample (right blue line) in the solid states using KBr pellets.

The characteristic absorption maxima around 390, 470, 590 nm are commonly observed for Mn^{II}-crystal sample (**3**·1.5CH_2Cl_2) and powder samples of Mn^{II}, Fe^{II}, Co^{II}, and Ni^{II}, and these spectral features indicate that these divalent metal cations interact with metalloligand $[Mo^{V}(mp)_3]^-$ by similar manner.

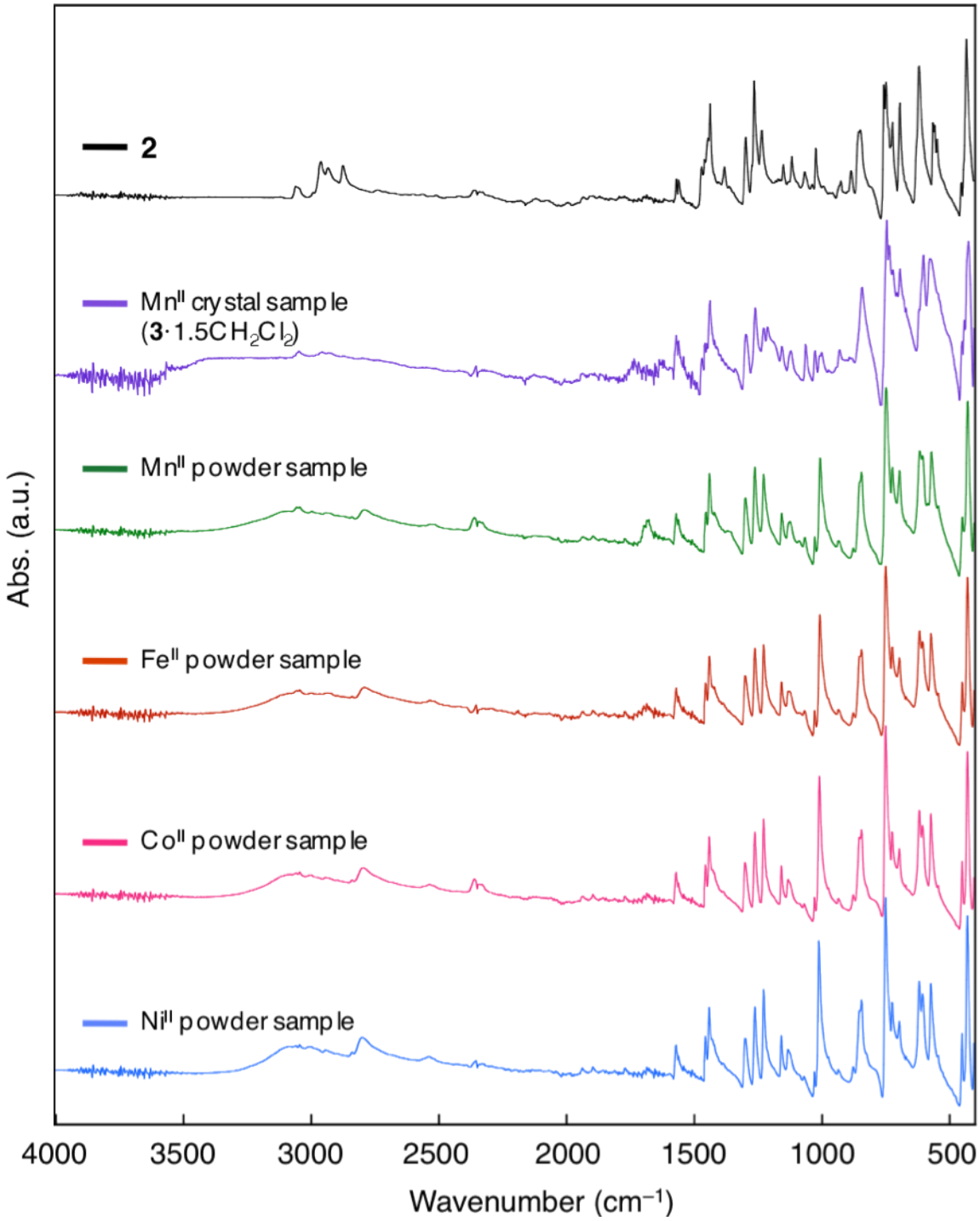

Figure 3S. IR spectra of **2** (black line), Mn^{II} crystal sample (**3**·1.5CH_2Cl_2) (purple line), Mn^{II} powder sample (green line), Fe^{II} powder sample (orange line), Co^{II} powder sample (pink line), and Ni^{II} powder sample (right blue line) in the solid states.

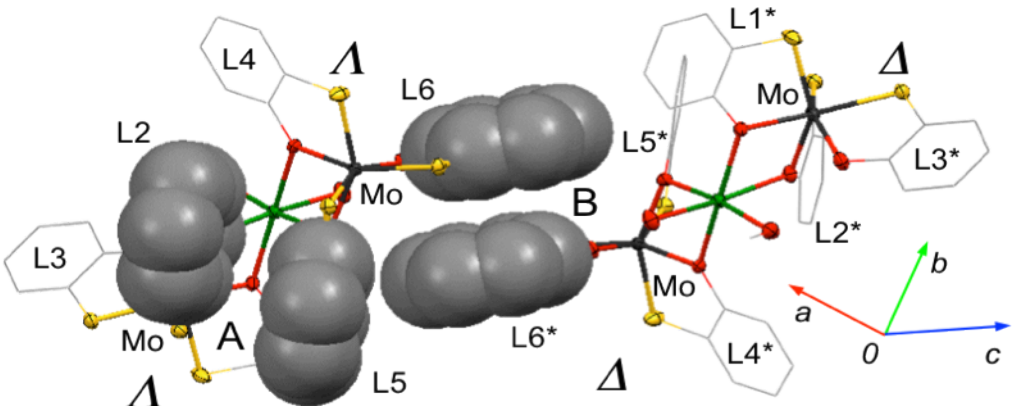

Figure 4S. Intramolecular (A) and intermolecular π–π interaction (B) in **3**·1.5CH_2Cl_2. CH_2Cl_2 molecules are omitted for clarity. The mp^{2-} rings (L2, L5, and L6) involved with π–π interactions are drawn as space-filling model.

In the cases of **3**·1.5CH_2Cl_2, *ΔΛ*-chirality around the pseudo-octahedral Mo^{V} centers is unified in trinuclear units (Figure 3S). The intramolecular π–π interaction with the shortest carbon atom distances among the aromatic rings are 3.450 Å (denoted as A) is found between neighboring *fac*-$[Mo(mp)_3]^-$ units through L2 and L5, both of which are involved in coordination to additional metal (Mn^{II}). Furthermore, the optically isomeric trinuclear units are alternately stacked between layers through intermolecular π–π interaction between L6 and L6* (denoted as B), which are free from additional metal binding, with the closest carbon atom distances 3.480 Å. Since the other mp^{2-} rings such as L1, L3, and L4 are not related with any intermolecular interaction, it is finally revealed that dimeric structures of trinuclear units through intermolecular π–π interaction are formed in crystals of **3**·1.5CH_2Cl_2.

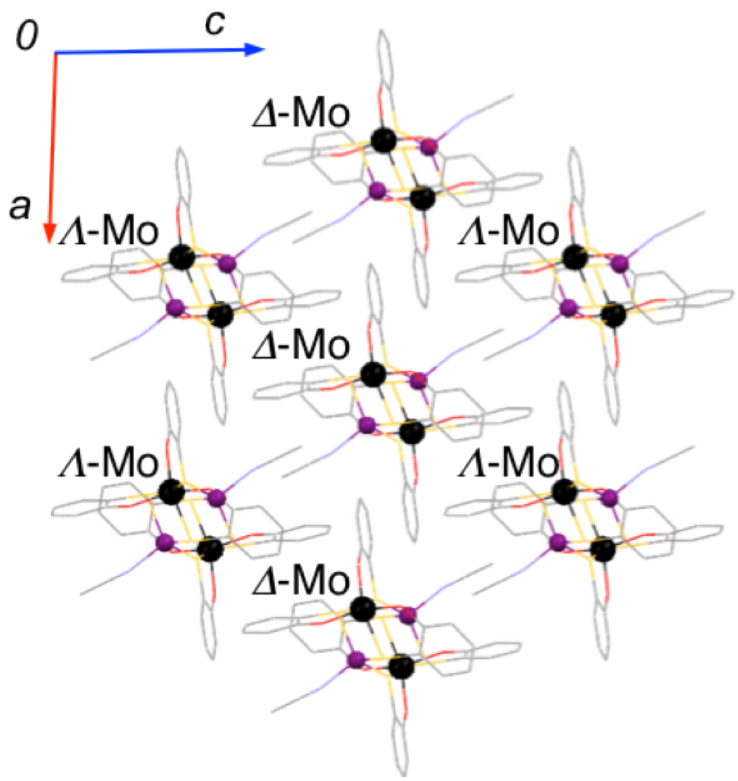

Figure 5S. Crystal packing of **5** projected along with the *b*-axis. The Mo and Cu atoms are drawn as ball and stick models, and, C, N, O, and S atoms are depicted as wireframe for clarity, with omission of hydrogen atoms.

Table 6S. UV-Vis-NIR spectroscopic data of **1**-**3**, and **5** in solution and in the solid states.

Complex	Condition	λ, nm (ε, $M^{-1}cm^{-1}$)					
1[a]	Solid	370[sh]	455	565	1186		
2[a]	Solid	370[sh]	421	494[sh]	590	680[sh]	1150
3[a]	Solid	370[sh]	470	590[sh]	730[sh]	1152	
5[a]	Solid	390[sh]	440	520	690[sh]	840[sh]	
1	CH_3CN	360(10800)	419(12500)	465(11000)[sh]	562(6960)[sh]	667(3590)[sh]	1052(790)
	o-$Cl_2C_6H_4$	370(11800)	444(15900)	568 (9840)[sh]	986(1860)		
2	CH_3CN	362(10900)	418(12600)	472(10800)[sh]	560(7090)[sh]	667(3640)[sh]	1052(790)
	o-$Cl_2C_6H_4$	367(12200)	420(14000)	470(11600)[sh]	562(7740)	667(3940)[sh]	1020(930)
3	CH_3CN	362(21500)[sh]	418(24800)	470(21500)[sh]	562(13900)[sh]	667(7120)[sh]	1052(1590)
	o-$Cl_2C_6H_4$	365(20600)[sh]	454(28900)	564(16400)[sh]	690(5510)[sh]	995(3800)	

[a] measured for KBr pellets. [sh] appeared as shoulder peak.

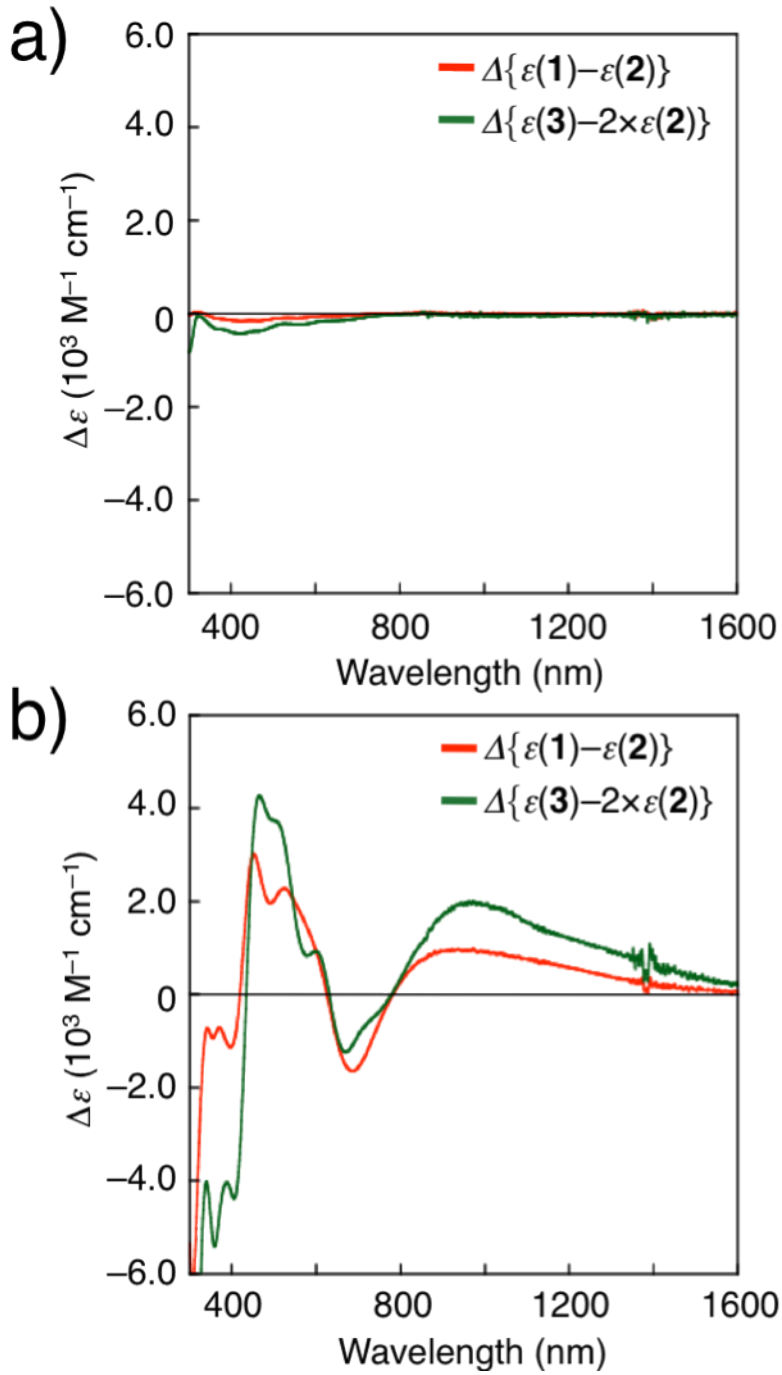

Figure 6S. Differential spectra of $\Delta\{\varepsilon(\mathbf{1})-\varepsilon(\mathbf{2})\}$ (red line) and $\Delta\{\varepsilon(\mathbf{3})-2\times\varepsilon(\mathbf{2})\}$ (green line) in (a) CH_3CN and (b) *o*-$Cl_2C_6H_4$ solution at 3×10^{-4} M at room temperature.

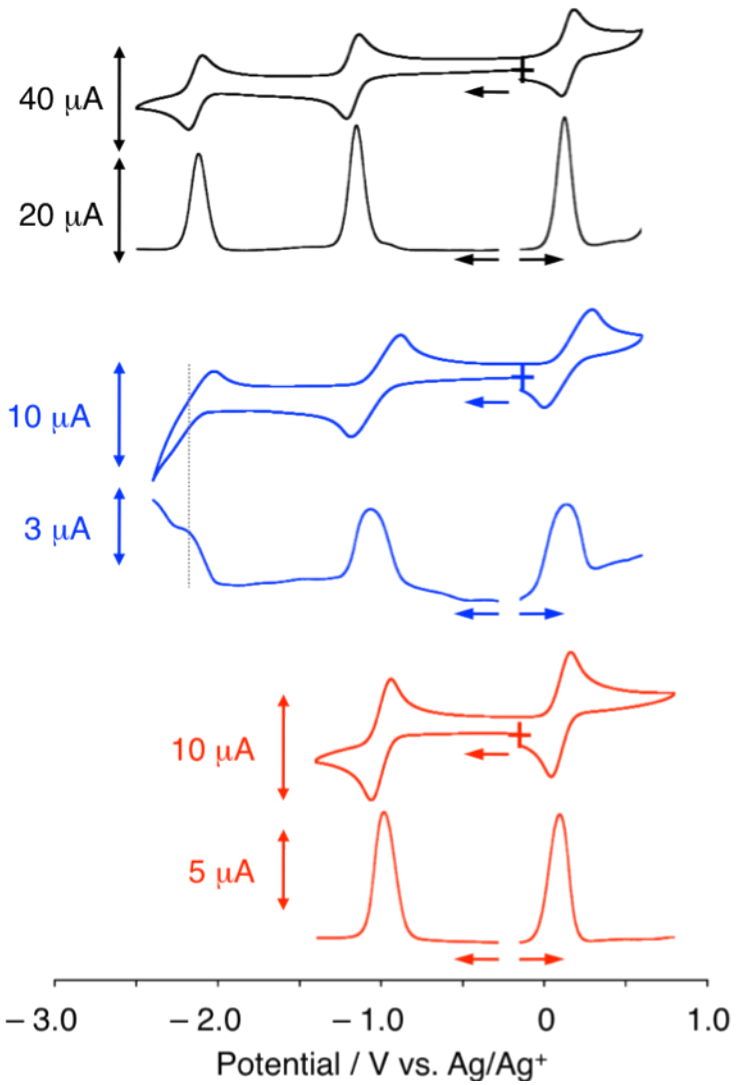

Figure 7S. CVs and DPVs of **2** (1×10^{-3} M) in CH_3CN with 0.05 M TBAP (black line), *o*-$Cl_2C_6H_4$ with 0.05 M TBAP (blue line), and *o*-$Cl_2C_6H_4$ with 0.05 M TBAFB (red line).

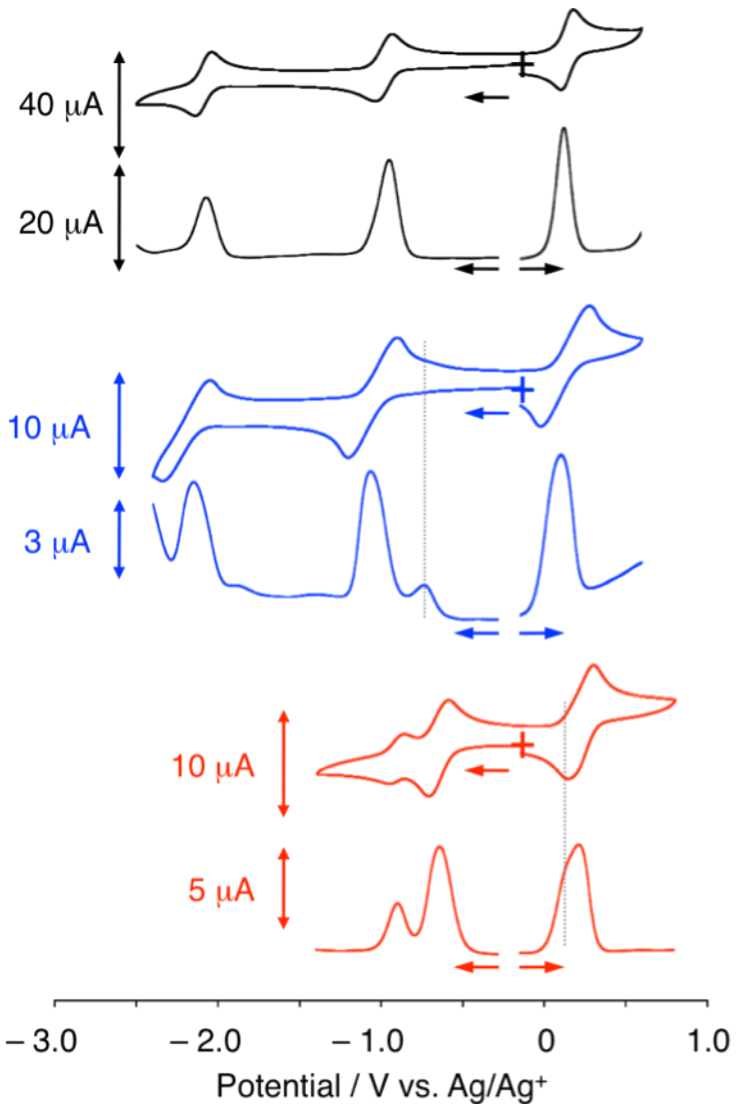

Figure 8S. CVs and DPVs of **1** (1×10^{-3} M) in CH_3CN with 0.05 M TBAP (black line), *o*-$Cl_2C_6H_4$ with 0.05 M TBAP (blue line), and *o*-$Cl_2C_6H_4$ with 0.05 M TBAFB (red line). For *o*-$Cl_2C_6H_4$ with TBAFB, negative region than –1.4 V could not be investigated due to its potential window.

The redox wave of **1** around –0.74 V indicates slight existence of assembly keeping associative interaction between the metalloligand and Na^+.

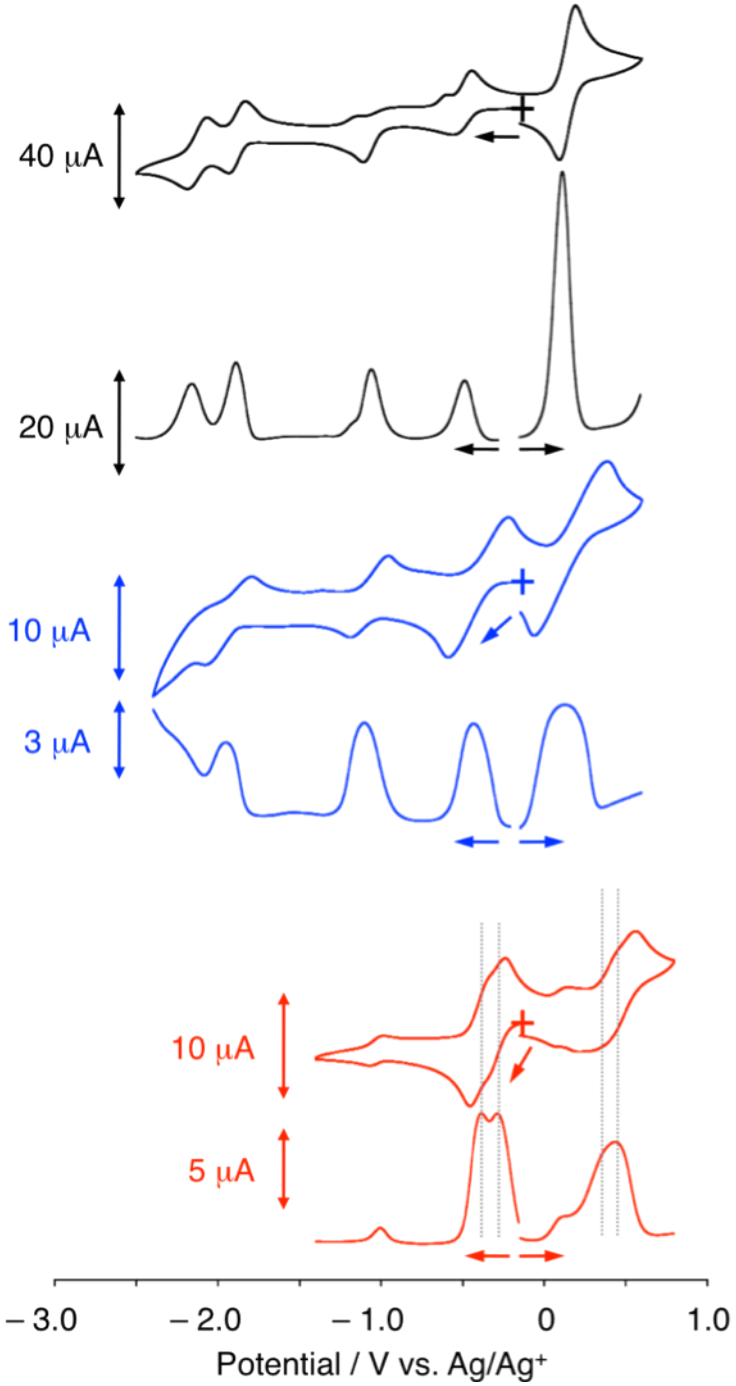

Figure 9S. CVs and DPVs of **3** (1×10^{-3} M) in CH_3CN with 0.05 M TBAP (black line), *o*-$Cl_2C_6H_4$ with 0.05 M TBAP (blue line), and *o*-$Cl_2C_6H_4$ with 0.05 M TBAFB (red line). For *o*-$Cl_2C_6H_4$ with TBAFB, negative region than –1.4 V could not be investigated due to its potential window.

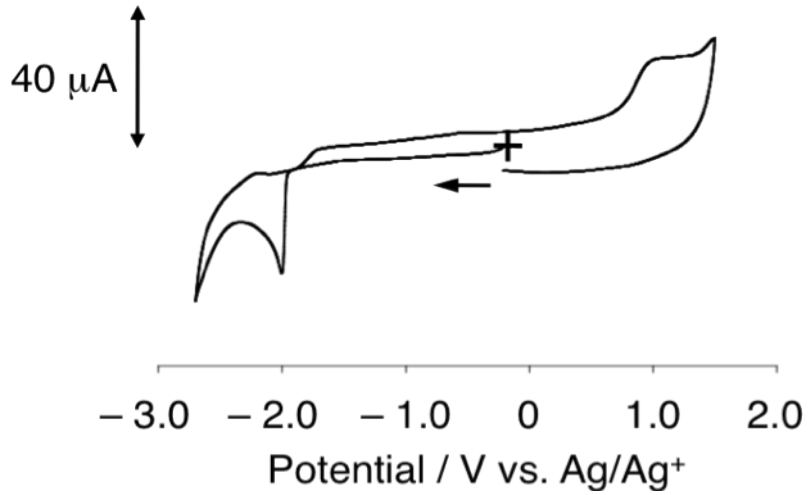

Figure 10S. CV of $Mn^{II}(H_2O)_6(ClO_4)_2$ (1×10^{-3} M) in CH_3CN with 0.1 M $TBAPF_6$.

Scheme 1S. Plausible mechanisms of electrochemically irreversible reactions of **3** in CH_3CN solution.[1]

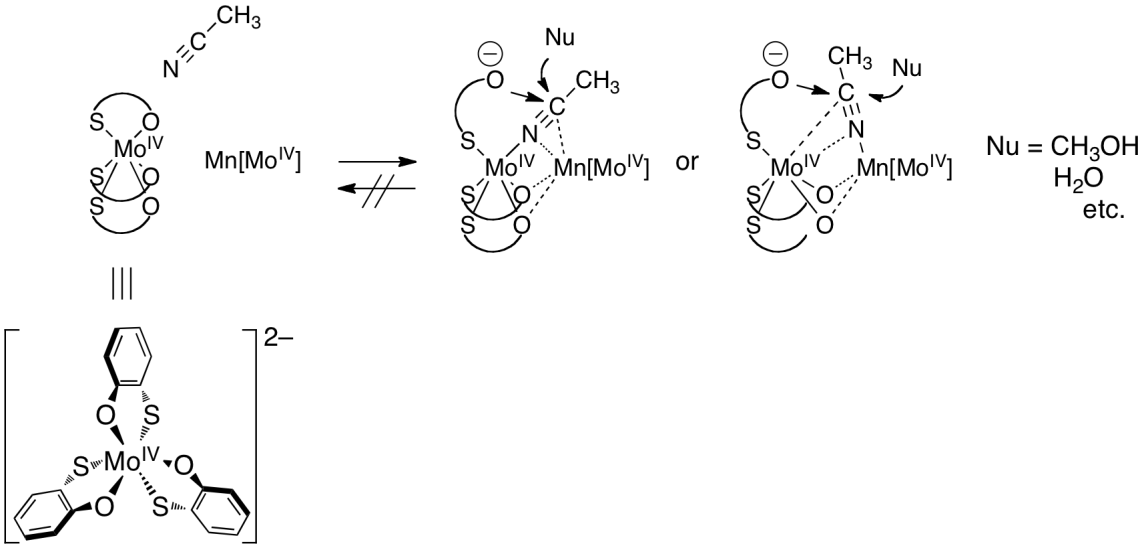

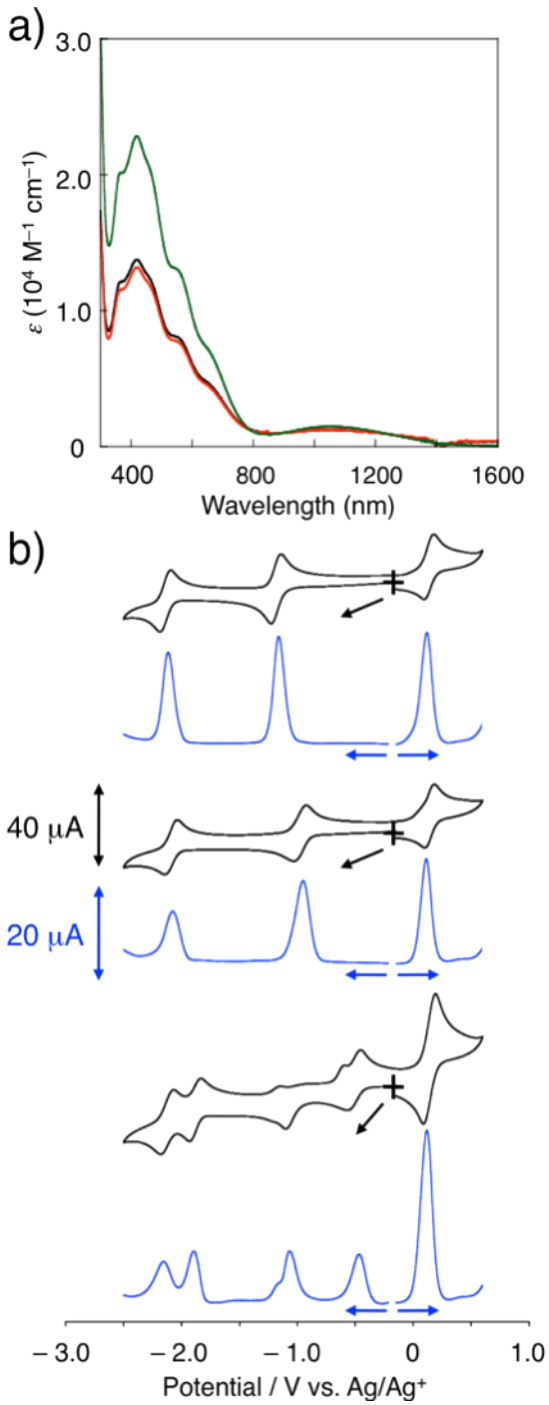

Figure 11S. (a) UV-Vis-NIR spectra of **1** (red line), **2** (black line), and **3** (green line) (3×10^{-4} M) in CH_3CN solution containing 1.5×10^{-2} M TBAFB. (b) CVs (black line) and DPVs (blue line) of **2** (top), **1** (middle), and **3** (bottom) (1×10^{-3} M) in CH_3CN solution containing 0.05 M TBAFB.

Table 7S. Redox potentials of **1**, **2**, and **3** in CH_3CN containing TBAFB.

Complex	vs. Ag/Ag^+		
	$E^{2}_{1/2}{}^{Red}$	$E^{1}_{1/2}{}^{Red}$	$E^{1}_{1/2}{}^{Ox}$
1	–2.09	–0.98	0.14
2	–2.14	–1.18	0.14
3	–1.14[irr]	–0.52	0.14

[irr] Irreversible; the recorded potentials are cathodic potentials at a scan rate of 50 mV/s.

References

1. (a) R. A. Michelin, M. Mozzon and R. Bertani, *Coord. Chem. Rev.*, 1996, **147**, 299-338; (b) V. Y. Kukushkin and A. J. L. Pombeiro, *Chem. Rev.*, 2002, **102**, 1771-1802.